Evolving corundum nanoparticles at room temperature

Hongbing Yang [a,1], Baoming Wang [b,1], Hong Zhang [c], Bing Shen [a], Yuanyuan Li [a], Ming Wang [a], Jianjun Wang [a], Wensheng Gao [d], Yueming Kang [a], Lu Li [a], Yanhao Dong [e,*], Jiangong Li [a,*], Ju Li [b,f,*]

[a] Institute of Materials Science and Engineering, School of Materials and Energy, Lanzhou University, Lanzhou 730000, China
[b] Department of Materials Science and Engineering, Massachusetts Institute of Technology, Cambridge, MA 02139, United States of America
[c] Electron Microscopy Centre of Lanzhou University, School of Materials and Energy, Lanzhou University, Lanzhou 730000, China
[d] College of Chemistry and Chemical Engineering, Lanzhou University, Lanzhou 730000, China
[e] State Key Laboratory of New Ceramics and Fine Processing, School of Materials Science and Engineering, Tsinghua University, Beijing 100084, China
[f] Department of Nuclear Science and Engineering, Massachusetts Institute of Technology, Cambridge, MA 02139, United States of America

ARTICLE INFO

ABSTRACT

Metals and ceramics in nanometric forms attract much attention due to their unique properties, yet their stability is often questioned. Nevertheless, the shape and size instabilities are thought to be suppressed at ambient conditions, especially for refractory materials with high melting points. Contrary to this notion, here we report gradual coarsening of sub-10 nm corundum (α-Al$_2$O$_3$) nanoparticles during room-temperature storage, indicating active surface diffusion at a surprisingly low temperature (13% of the absolute melting point). Prolific surface diffusion is confirmed by in-situ transmission electron microscopy mechanical deformation, performed at room temperature and demonstrating remarkable high-strain-rate Coble pseudoelasticity. Anomalously small activation energy and growth stagnation are found in high-temperature coarsening experiments, suggesting additional chemical driving forces beyond purely physical capillarity. We expect similar phenomena may also exist in other ceramic materials, which is an important factor to consider for quality control, storage, and applications of ultrafine nanomaterials.

1. Introduction

Corundum, α-Al$_2$O$_3$, is a high-melting-point material with various applications as structural ceramics, refractories, and catalyst supports [1–8]. It is the thermodynamically stable phase of alumina polymorphs [9–12], and many applications critically rely on its high-temperature stability and chemical inertness. Ultrafine α-Al$_2$O$_3$ nanoparticles with high sinterability and large surface area are long sought for ceramic processing and catalysis, yet the synthesis remains challenging. The reason is that low-temperature synthesis often results in metastable phases such as γ- and θ-Al$_2$O$_3$, and their conversion to α-Al$_2$O$_3$ requires high temperature (>~1100 °C) to overcome the large kinetic barrier, which unavoidably coarsens the particle size [13–16]. This challenge has recently been addressed by either mechanochemical method [17,18] or direct milling of coarse α-Al$_2$O$_3$ powders [19,20], and high-purity disperse α-Al$_2$O$_3$ nanoparticles with tunable sizes down to 3.3 nm

have been successfully produced [19]. It directly enables pressureless sintering of dense nanocrystalline Al$_2$O$_3$ ceramics [21–24], and the superior stability of high-surface-area α-Al$_2$O$_3$ support has also been demonstrated under harsh hydrothermal conditions (at 150 °C = 423 K) for Fischer-Tropsch synthesis [25]. The latter stability is not totally unexpected considering the high melting point of Al$_2$O$_3$ (T_m=2072 °C = 2345 K) and the phase stability of α-Al$_2$O$_3$.

Against the above background on the stability of refractory α-Al$_2$O$_3$, we recently found remarkably active surface kinetics of sub-10 nm α-Al$_2$O$_3$ nanoparticles at room temperature (~0.13T_m), which form aggregates with strong inter-particle bonding (sometimes quoted as "sintering neck") and gradually coarsen during extended-time storage from months to years. The formation of aggregates is known for ceramic nano powders, and it severely affects the sinterability of ultrafine powders. In our case, we first noted different sintering results of similarly processed green bodies using as-synthesized and ambient-

condition stored α-Al$_2$O$_3$ nanoparticles. (The prolonged storage was accidental due to much-delayed experiments during covid-19 pandemic.) The former powder can be sintered to ~90% relative density (average grain size G_{avg}=42 nm, Fig. 1a) at 1150 ^{o}C without holding and two-step sintered to 99% relative density (G_{avg}=39 nm, Fig. 1b) at 1100 ^{o}C without holding and then at 975 ^{o}C for 40 h. In comparison, sintering the latter powder at 1150 ^{o}C without holding results in only ~80% relative density and larger G_{avg}=114 nm (Fig. 1c). The lowered density is apparently due to aggregation of the powders and the larger G_{avg} is due to localized sintering and subsequently accelerated grain growth without pore pinning. Interestingly, close inspections of the stored α-Al$_2$O$_3$ nanoparticles revealed unexpected coarsening, i.e., particle growth that requires active surface diffusion. This motivates the present study, which reports the morphological evolution, especially the coarsening kinetics, of α-Al$_2$O$_3$ nanoparticles at room temperature. We further confirmed the active surface diffusion by room-temperature in-situ transmission electron microscopy (TEM) deformation, which shows remarkable high-strain-rate (~0.01 s^{-1}) pseudoelasticity in real-time. We found anomalously small activation energy (~0.25 eV) and growth stagnation in high-temperature coarsening experiments, suggesting additional driving force beyond classical physical capillarity. The influence of surface chemical adsorption and the implications on other materials will be discussed. To this end, we expect similar surface-diffusion-mediated physical processes in other ceramic nanostructures, enabling novel processing and designs at the nanoscale (e.g., cold welding with or without chemical "solder" [26,27]).

2. Experimental methods

α-Al$_2$O$_3$ nanoparticles were prepared by ball milling, followed by acid corrosion and centrifuge separation [19]. Micron-size high-purity (99.999%) α-Al$_2$O$_3$ powders were ball-milled under 250 rpm for 20 h using stainless-steel grinding balls and jars. The milled powders were corroded in 12 mol L^{-1} hydrochloric acid (HCl) at room temperature for 10 h, and then separated using different concentrations of HCl solutions and centrifuge-collected using 12 mol L^{-1} HCl as the coagulation agent. By adjusting the concentration of HCl in the separation step, α-Al$_2$O$_3$ nanoparticles with different sizes were obtained. The obtained α-Al$_2$O$_3$ nanoparticles have >99.9% purity as we characterized previously [22]. For acid etching process of the stored α-Al$_2$O$_3$ nanoparticles or those after heat treatment, the samples were etched using 4 mol L^{-1} HCl in ultrasonic bath at room temperature and then centrifuge-collected at 15,000 rpm. The acid etching process was completed within one hour and it does not affect the size and crystallinity of α-Al$_2$O$_3$ nanoparticles.

A phase of the α-Al$_2$O$_3$ nanoparticles was characterized by X-ray diffraction (XRD) on Rigaku D/max-2400 diffractometer with Cu K_α radiation under 40 kV and 100 mA. The fractured surfaces of the sintered samples were characterized by scanning electron microscopy (SEM; Tescan LYRA3 XMU). Morphology, high-resolution transmission electron microscopy (HRTEM) and selected area electron diffraction (SAED) of α-Al$_2$O$_3$ nanoparticles were characterized by transmission electron microscopy (TEM; FEI Tecnai G2 F30, FEI, USA) and Cs-TEM

(Spectra 300, Thermo Fisher Scientific Inc., USA) operated under 300 kV. Thermogravimetric analysis (TGA) was conducted in air at 5 $^{\circ}$C min^{-1} on Perkin-Elmer Pyris Diamond thermal analyzer. Temperature-programmed in-situ diffuse reflectance infrared Fourier transform (DRIFT) spectra were measured on Bruker Invenio® spectrometer equipped with a detector for Fourier transform spectroscopy (DTGS detector) and a Harrick high-temperature environmental chamber with ZnSe windows. The samples were first purged at 30 $^{\circ}$C for 10 min in flowing Ar (flow rate: 10 ml min^{-1}), and then heated to 390 $^{\circ}$C at 5 $^{\circ}$C min^{-1}. An infrared Fourier (IR) spectrum was collected every 5 $^{\circ}$C during heating.

For in-situ TEM deformation, α-Al$_2$O$_3$ nanoparticles (NP#8) were dispersed in deionized water in ultrasonic bath at room temperature for 45 min to form a suspension with a particle concentration of 0.05 g L^{-1}. W tips were prepared by electro-chemical etching using 2 mol L^{-1} NaOH solution. α-Al$_2$O$_3$ nanoparticles were loaded onto a carrier W tip (top W tip in Fig. 4) by dipping the tip in the suspension of α-Al$_2$O$_3$ nanoparticles for ~1 s, followed by natural drying in air. Two W tips were accommodated in a customer-modified Nanofactory TEM holder (Supplementary Figure S1). In-situ deformation experiments were conducted in JEOL 2010F TEM under an acceleration voltage of 200 kV. A dose-rate experiment was carried out to obtain low-dose-rate imaging to minimize the electron beam effects.

3. Room-temperature coarsening

We synthesized dispersed ultrafine α-Al$_2$O$_3$ nanoparticles by ball-milling micron-size high-purity α-Al$_2$O$_3$ powders, followed by acid leaching (for impurity removal) and corrosion (for dispersion), separation, and centrifuge collection [19]. Examples of the as-synthesized pristine α-Al$_2$O$_3$ nanoparticles are shown in Fig. 2a for NP#1 with an average particle size d_{avg}=3.4 nm (size distribution plotted in Fig. 2d in red), and Fig. 2e for NP#2 with d_{avg}=5.0 nm and a narrow size distribution (size distribution plotted in Fig. 2h in red). (See Supplementary Note S1 for the measurement/statistics methods of particle size and size distribution, and Supplementary Figure S2 for an example of the measurement process.) However, notable differences were found after extended-time storage at ambient conditions (both powders were stored in closed plastic centrifuge tubes in the laboratory). After 730 days of ambient-condition storage, the initially dispersed α-Al$_2$O$_3$ nanoparticles (which form soft agglomerates and can be easily separated by ultrasonic treatment and electron beam during TEM measurements) form partially densified aggregates (Fig. 2b for NP#1 and Fig. 2f for NP#2), where strongly bonded particles can no longer be easily separated. We confirmed no phase transition took place and both NP#1 and NP#2 remained in the α phase after storage (see XRD, data in Supplementary Figure S3). To quantify the coarsening, the aggregates were etched in acid at room temperature, which was able to separate the particles (well dispersed after etching, as shown in Fig. 2c for NP#1 and Fig. 2g for NP#2) without causing any size change. (Control experiments to exclude etching-induced size change were conducted. α-Al$_2$O$_3$ nanoparticles have the same d_{avg}, size distribution, and crystallinity before
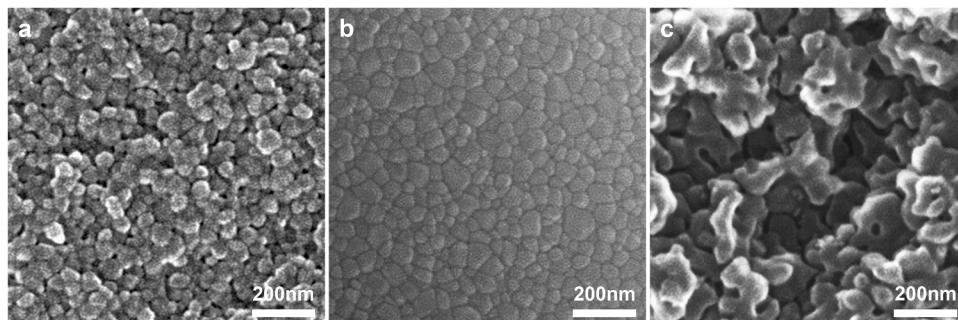

Fig. 1. Microstructure of sintered Al$_2$O$_3$ ceramics. (a) Partially sintered sample using as-synthesized α-Al$_2$O$_3$ nanoparticles by heating to 1150 ^{o}C without holding (ramping and cooling rate: 5 ^{o}C min^{-1}). (b) Fully sintered sample using as-synthesized α-Al$_2$O$_3$ nanoparticles by first heating to 1100 ^{o}C without holding (ramping rate: 5 ^{o}C min^{-1}), then cooling to 975 ^{o}C (cooling rate: 10 ^{o}C min^{-1}) and holding for 40 h (cooling rate: 5 ^{o}C min^{-1}). (c) Partially sintered sample using covid-19 stored α-Al$_2$O$_3$ nanoparticles (at room temperature for 730 days) by heating to 1150 ^{o}C without holding (ramping and cooling rate: 5 ^{o}C min^{-1}).
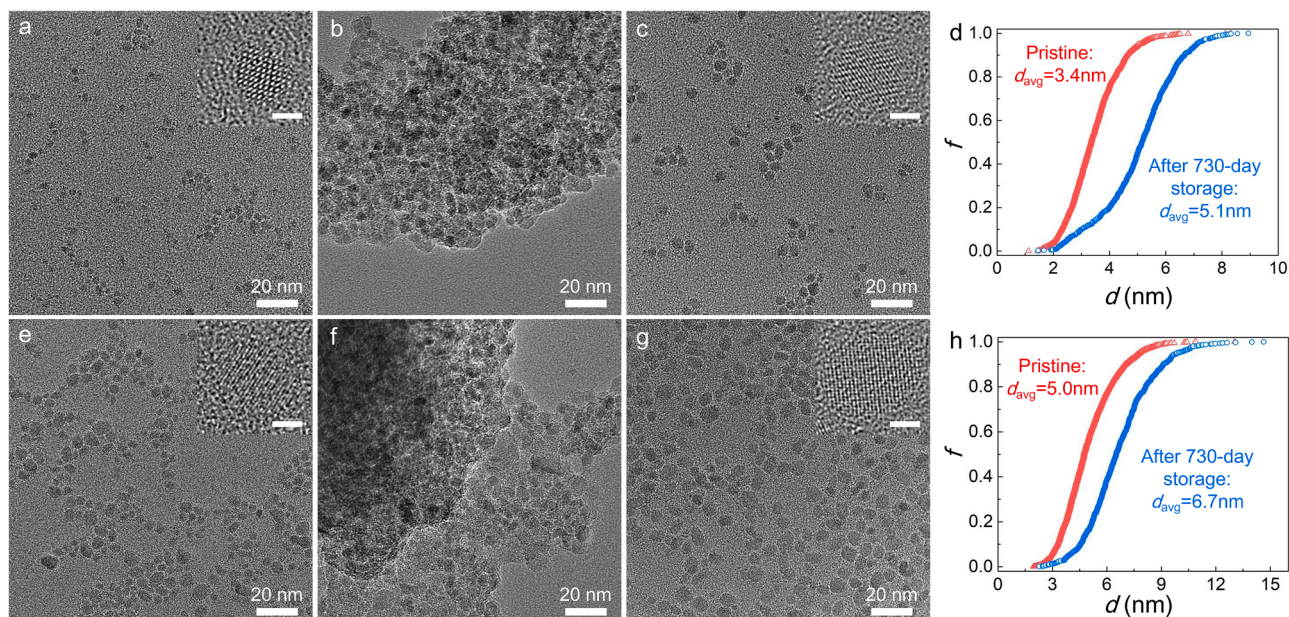
Fig. 2. Room-temperature coarsening of stored α-Al$_2$O$_3$ nanoparticles. (a-c) Morphology of pristine NP#1 (a), and 730-day stored NP#1 before (b) and after (c) acid etching. (d) Particle size distributions of pristine and 730-day stored NP#1. (e-g) Morphology of pristine NP#2 (e), and 730-day stored NP#2 before (f) and after (g) acid etching. (h) Particle size distributions (accumulative fraction f vs. particle size d) of pristine and 730-day stored NP#2. The inset of (a), (c), (e) and (g) show HRTEM images of the corresponding α-Al$_2$O$_3$ nanoparticles (scale bar, 2 nm).

and after the same acid etching process as shown in Supplementary Figure S4.) Measurements on the etching-separated particles show a definite size increase, from d_{avg}=3.4 nm to 5.1 nm (50% increase) for NP#1 and from 5.0 nm to 6.7 nm (34% increase) for NP#2 after 730-day storage (their size distributions shown in Fig. 2d and 2h in blue, respectively).

We confirmed that the room-temperature coarsening is a general phenomenon for other batches of synthesized α-Al$_2$O$_3$ nanoparticles with d_{avg} ranging from 4.0 nm to 10.5 nm. Examples (Fig. 3) include: (1) NP#3 with initial d_{avg}=3.7 nm coarsens to d_{avg}=5.7 nm after 850 days; (2) NP#4 with initial d_{avg}=5.2 nm coarsens to d_{avg}=6.7 nm after 960 days; (3) NP#5 with initial d_{avg}=6.7 nm coarsens to d_{avg}=8.6 nm after 850 days; (4) NP#6 with initial d_{avg}=6.3 nm coarsens to d_{avg}=8.5 nm after 730 days; (5) NP#7 with initial d_{avg}=10.5 nm coarsens to d_{avg}=11.2 nm after 730 days; (6) NP#8 with initial d_{avg}=4.0 nm coarsens to d_{avg}=4.8 nm after 133 days, to 5.2 nm after 313 days, and to 5.3 nm after 382 days; (7) NP#9 with initial d_{avg}=4.3 nm coarsens to d_{avg}=4.7 nm after 140 days, to 5.5 nm after 325 days, and to 5.7 nm after 390 days. In addition, after storage, we noted a monotonic decrease in

Fig. 3. Room-temperature coarsening of variously produced α-Al$_2$O$_3$ nanoparticles. Comparison of the average particle size d_{avg} of NP#3 to NP#9 before and after storage.

both the standard deviation σ of the normalized size distribution (i.e., narrowed size distribution) and the average aspect ratio of the particles (i.e., improved particle sphericity). (Detailed data are summarized in Supplementary Table S1. The skewness of the normalized particle size distribution is also listed, but no clear trend has been identified.) Interestingly, exceptionally small σ=0.20 was obtained for NP#1 after 730-day storage, which is even smaller than σ=0.215 for the theoretical size distribution given by Lifshitz, Slyozov, and Wagner (LSW) for Ostwald ripening [28,29]. We confirmed that phase of these batches of nanoparticles also did not change after storage and remained in the α phase. By comparing the XRD patterns of as-synthesized and stored nanoparticles, we found that the crystallinity of the nanoparticles improved and the micro-strain ε decreases after storage. For example, for NP#8, the intensity of (2 1 4) peak at 2θ around 66.5° increases after 382-day storage (Supplementary Figure S5) and micro-strain ε decreases from 7.19×10^{-3} in the as-synthesized state to 5.93×10^{-3} after 133 days and to 4.86×10^{-3} after 313 days (See Supplementary Note 2 for the detailed calculation method.).

We used the following two supportive methods to track the coarsening. First, we calculated the average grain size D from the peak broadening of the XRD data. (See Supplementary Note 2 for the detailed calculation method and Supplementary Figure S6 for an example of the calculation process. This method is only supportive and not preferred because of possible micro-strain.) The results in Supplementary Table S2 show that the D of α-Al$_2$O$_3$ nanoparticles increased after storage, e.g., NP#8 with initial D = 4.2 nm increases to D = 4.6 nm after 133 days, to 4.8 nm after 313 days, and to 4.9 nm after 382 days. Second, we calculated D from specific surface areas S_{BET} measured by Brunauer-Emmett-Teller (BET) method. (See Supplementary Note 3 for the details. This method is only supportive and not preferred because of agglomerations of ultra-fine nanoparticles.) The results in Supplementary Table S3 show that the S_{BET} of α-Al$_2$O$_3$ nanoparticles decreased sharply after storage and without acid etching (mainly due to aggregation), and even after the acid etching process, the S_{BET} still showed a decrease (caused by coarsening). For example, NP#1 with initial S_{BET}=210 m^2/g decreased to 117 m^2/g without acid etching and 187 m^2/g after acid etching after 730-day ambient-condition storage.

Based on the above results, we conclude that sub-10 nm α-Al$_2$O$_3$
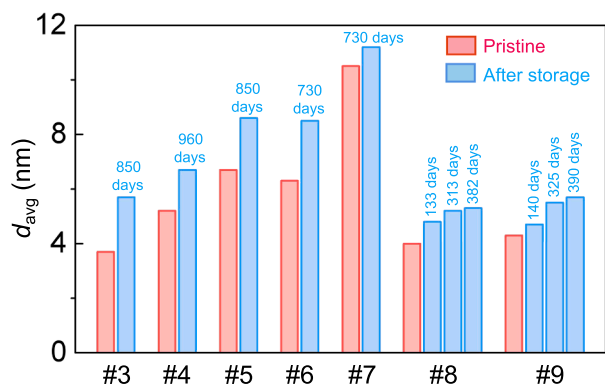
nanoparticles indeed undergo aggregation, coarsening and shape changes—slow yet still pronounced over an extended time of months to years—at ambient conditions. Since the α-Al$_2$O$_3$ nanoparticles were stored in powder form and not in any solutions, it demonstrates active surface diffusion at room temperature, which is as low as $\sim$0.13T_m of Al$_2$O$_3$. (In addition to surface diffusion enabled particle coarsening, diffusionless oriented attachment could be another coarsening mechanism, especially for nanoparticles with large contact stresses. However, because the average aspect ratio of the particles decreased after storage as shown in Supplementary Table S1, diffusionless oriented attachment that would increase the aspect ratio of the particles [30] should not be the primary mechanism for coarsening in our experiments.) This finding is especially surprising because Al$_2$O$_3$ is known for the sluggish grain boundary and lattice diffusivity even at elevated temperatures (e.g., >1000 °C) [31–37], which makes Al$_2$O$_3$ ceramics difficult to sinter and Al$_2$O$_3$ scale useful to protect high-temperature alloys.

4. In-situ room-temperature deformation

We next proved the active room-temperature surface diffusion by an in-situ deformation experiment inside TEM. Surface-diffusion-mediated pseudoelasticity has been previously reported in Ag nanoparticles [38], where sub-10 nm single crystal of Ag can be deformed pseudoelastically upon loading and recover its original shape after unloading that minimizes the surface energy (thus not plastic deformation). The process can take place at room temperature ($\sim$0.24T_m of Ag) in real time because the strain-rate of Coble pseudoelasticity scales with (size)$^{-3}$, and the surface diffusion activation energy may also be particle curvature dependent, which enable extremely high strain rate and low temperature for ultrafine nanoparticles. Therefore, we decided to conduct similar experiments on our sub-10 nm α-Al$_2$O$_3$ nanoparticles, albeit room temperature means even a much lower homologous temperature for Al$_2$O$_3$ than Ag. (Room temperature is $\sim$0.13T_m of Al$_2$O$_3$, and 0.13T_m of Ag is 161 $K=-112$ °C.) Fig. 4a shows a $\sim$5 nm α-Al$_2$O$_3$ nanoparticle (NP#8) loaded on a tungsten (W) tip on the top and a to-be-loaded W tip on the bottom. When the bottom W tip started to contact the α-Al$_2$O$_3$ nanoparticle in Fig. 4b, the nanoparticle experienced a mixed compression and shear force and was deformed. The deformation became larger in Fig. 4c-d as the bottom W tip displaced further with respect to the top W

tip, setting a strain of $\sim$80–100% for the nanoparticle. The "loading" process from Fig. 4b to 4d took $\sim$100 s, thus the estimated strain rate is roughly on the order of 0.01 s^{-1}. During "unloading" (Fig. 4e-h), when the tip moved back to its original position, the nanoparticle changed its shape to a less deformed state (Fig. 4f). Afterwards, the nanoparticle was still partially bonded to the bottom W tip and kept deforming along with the moving direction of the tip and in the opposite direction of the "loading" cycle (Fig. 4g). Eventually, the nanoparticle was detached from the bottom tip and rapidly relaxed from the highly deformed shape towards its original shape (Fig. 4h). The entire deformation cycle was recorded in Supplementary Video S1.

The observations above are clearly not plastic deformation, as the unloaded nanoparticle relaxes its shape regardless of the huge strains during the loading process. The nanoparticle does not fracture either, even though severe deformation, large shear strain, and high strain rate are all involved. Such a low-temperature pseudoelasticity has not been observed for α-Al$_2$O$_3$ (whose ultrafine nanoparticle form has only been synthesized recently), neither in other ceramic materials to the best of our knowledge. While we acknowledge electron beam radiation may have some effects (e.g., accelerating the surface diffusion) and is difficult to be completely ruled out, we confirmed the shape and crystallinity α-Al$_2$O$_3$ nanoparticles are stable under the employed beam conditions (Supplementary Video S2). Therefore, we expect the observations to be valid and relevant to similar deformation conditions. Meanwhile, it should be pointed out that the Coble pseudoelasticity observed here relies on surface diffusion of crystalline α-Al$_2$O$_3$ particles (each particle is a small piece of single crystal). It is different from the diffusion and deformation mechanisms of amorphous Al$_2$O$_3$, whose thin-film form has been reported to be plastically deformable at room temperature [39,40].

5. Higher-temperature coarsening kinetics

To better understand the underlying mechanism, we conducted high-temperature annealing experiments in air to investigate the coarsening kinetics of NP#8. (A different batch of NP#8 was used in this section, which has an initial d_{avg}=4.1 nm.) Fig. 5a shows d_{avg} of as-synthesized α-Al$_2$O$_3$ particles before and after heat treatment at 100 °C, 150 °C, 200 °C, and 250 °C for different times. (Detailed morphologies and size distributions are plotted in Supplementary Figure S7. Selected XRD data
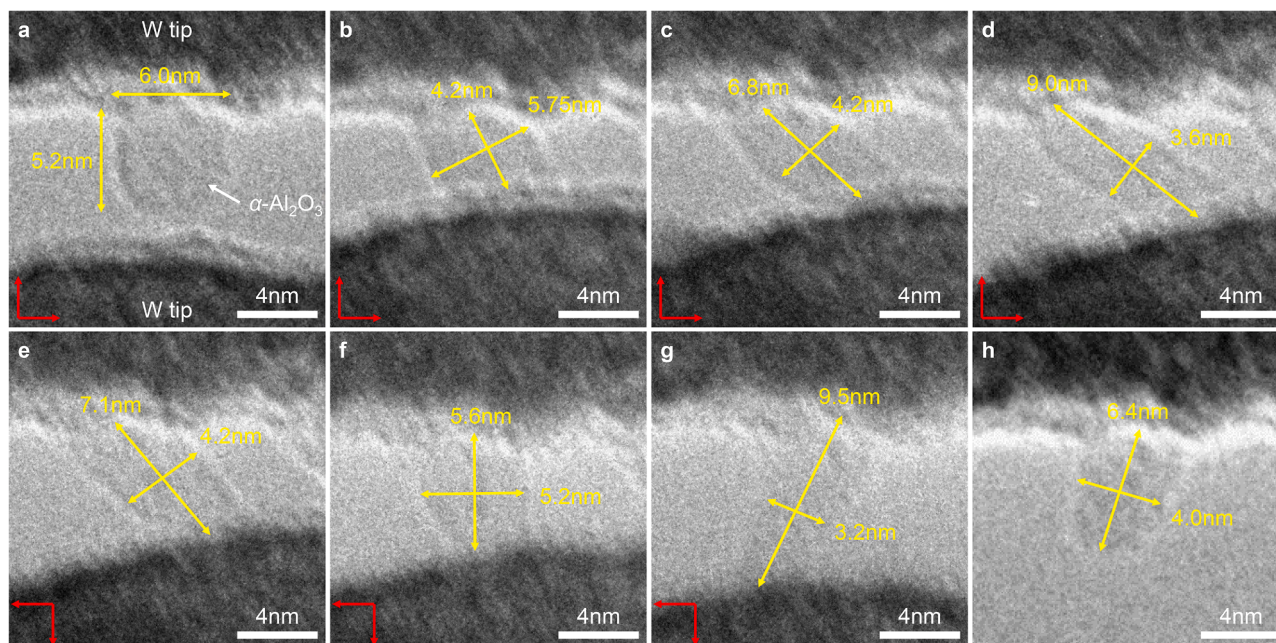

Fig. 4. Pseudoelastic deformation of α-Al$_2$O$_3$ nanoparticles. (a) Initial configuration before loading. (b-g) Dynamic shape evolution during loading (b-d) and unloading (e-g). (h) Configuration after unloading. Red arrows on the bottom-left denote the moving direction of the bottom W tip with respect to the top W tip.
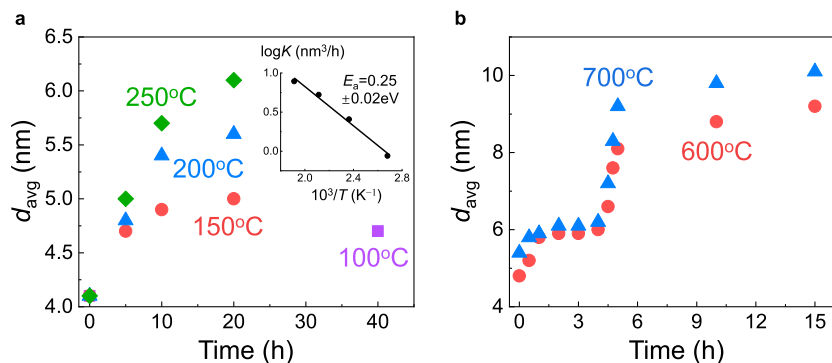
Fig. 5. High-temperature coarsening kinetics of α-Al$_2$O$_3$ nanoparticles. (a) Average particle size vs. annealing time at 100 °C, 150 °C, 200 °C, and 250 °C. (b) Average particle size vs. annealing time at 600 °C, and 700 °C. Inset of (a): Arrhenius plot of the calculated kinetic parameter K.

as well as the calculated average grain sizes are plotted in Supplementary Figure S8 and summarized in Supplementary Table S4, respectively, all of which show α phase.) We tried to fit the data at 150–250 °C using cubic growth law for the classical Ostwald ripening process

$$d_{avg}^3 - d_{avg,0}^3 = Kt = K_0 exp(-E_a / k_B T)t \qquad (1)$$

where $d_{avg,0}$ is the average particle size before heat treatment, t is the time, K is a kinetic parameter with an Arrhenius form, K_0 and E_a are the pre-exponent factor and activation energy of K, respectively, k_B is the Boltzmann constant, and T is the absolute temperature. However, the data of d_{avg}^3 do not show good linearity (Supplementary Figure S9) and growth stagnation can be clearly seen in both d_{avg}-t plot in Fig. 5a and d_{avg}^3-t plot in Supplementary Figure S9. Nevertheless, we proceeded with Eq. (1) to calculate $K(T)$ (inset of Fig. 5a, 100 °C data also included) and analyzed the temperature dependence. It gives anomalously small activation energy of 0.25±0.02 eV, too small to account for any mass diffusion process via surface, grain boundaries, or lattice of Al$_2$O$_3$. (For example, activation energy in the range of 3.2–9.2 eV for oxygen grain boundary diffusion, 4.6–4.8 eV for pipe diffusion, 4.2–8.6 eV for creep, and 3.2–6.5 eV for sintering; for more details, see Ref. [24] and [37].) It may be related to some non-classical mechanisms such as the motion of clusters on the surface [41,42], solution (adsorbed water)-enhanced surface diffusion [43,44], surface/lattice structural change driven coarsening [45,46], which have different temperature dependence and different growth law. On the other hand, such a weak temperature dependence shares similarities with cold sintering experiments [47], where large applied stresses and long holding time result in relatively low-temperature densification (e.g., at 150–200 °C) with the aid of solvents (e.g., water).

Annealing data at higher temperatures of 600 °C and 700 °C reveal another striking feature. As shown in Fig. 5b, at both temperatures, d_{avg} grows rapidly in the first hour, then saturates to a plateau at ~6 nm until 4 h, next transits to another fast-growing stage at ~4–5 h to ~8 nm at 600 °C and ~9 nm at 700 °C, and finally reaches a second stagnated stage after 5 h. (Detailed morphologies and size distributions are plotted in Supplementary Figure S10–11. Selected XRD data as well as calculated average grain size D are plotted in Supplementary Figure S12 and summarized in Supplementary Table S4, respectively, all of which show α phase.) The transition in coarsening kinetics at 4–5 h suggests a possible change in the growth mechanism, which we believe is due to the removal of chemically adsorbed (chemisorbed) water species and the change in surface structure (details shall be discussed in the following section). Before this potential desorption event, the 600 °C and 700 °C annealed nanoparticles have similar d_{avg} of ~6 nm at the plateau at 1–4 h. This relatively athermal observation is consistent with the small activation energy found in 100–250 °C annealing experiments. Higher-temperature annealing experiments (e.g., at 800 °C) resulted in substantial sintering, after which individual particles can no longer be

separated by the etching process. We therefore did not proceed further.

6. Surface adsorption and desorption

Ultrafine nanoparticles with large surface areas are known to adsorb a substantial amount of water at ambient conditions. To quantify the amount of the adsorbed water, we conducted TGA for both the pristine and the 505-day stored NP#8. As shown in Fig. 6a, both samples show continuous weight loss up to 800 °C. The total weight loss is 21.6 wt% for the pristine sample and 21.7 wt% for the stored sample. Using a spherical model with 4.0 nm diameter and 3.96 g cm^{-3} theoretical density for α-Al$_2$O$_3$ nanoparticles and 1.0 g cm^{-3} density for adsorbed water species, we estimate 21.6–21.7 wt% water corresponds a water adsorption layer of ~0.6 nm in thickness on the surface. This is much beyond monolayer coverage. Furthermore, as the physically adsorbed (physisorbed) water species are expected to be removed at lower temperatures than the chemically adsorbed ones, we noted the weight loss of the stored sample shifts to higher temperature than the pristine sample, thus having more chemically adsorbed water. This also supports the active surface relaxation during storage. Meanwhile, the smooth weight loss curves do not have obvious loss peaks, which seems to suggest the adsorption strength has a continuous distribution and there might not be a definite boundary between physical and chemical adsorptions of the ultrafine α-Al$_2$O$_3$ nanoparticles. Lastly, we conducted in-situ DRIFT spectroscopy to characterize the stored NP#8. Fig. 6b shows DRIFT spectra as a function of the measurement temperature T from 40 °C to 390 °C. While the physically adsorbed water molecules (characterized by the broad peak at 3321 cm^{-1} [48–50]) rapidly weakens at 40–100 °C, the strong peak at 3724 cm^{-1} assigned to isolated hydroxyl groups [48–52] (a form of chemically adsorbed water species) exists up to the highest measurement temperature of 390 °C (it has little changes beyond 260 °C, which indicates strong chemical adsorption). These results are consistent with the physical picture presented in the literature for surface adsorption of α-Al$_2$O$_3$, which has an intermediate surface structure between α-Al$_2$O$_3$ and γ-Al(OH)$_3$ and a surface termination of monolayer -OH group, followed by molecularly adsorbed water in a partially order overlayer on top of the -OH group terminated surface [50,52-54]. The existence of strong chemical adsorption above 390 °C from DRIFT and the continuous weight loss up to 800 °C from TGA also support a possible final-step desorption and surface relaxation/reconstruction after hours' annealing at 600 °C and 700 °C, which may explain the growth transition in Fig. 5b.

7. Discussions

Room-temperature coarsening of oxide nanoparticles has been previously reported in ZnO [55], a functional ceramic used in electronics, sensing and optics [56,57]. The pristine ZnO nanoparticles grew from 11.7 nm to 15.6 nm after 175 days at room temperature. Growth
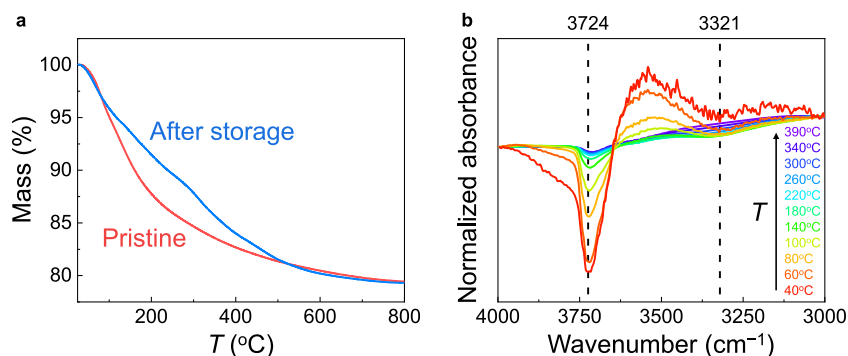
Fig. 6. Characterizations of surface adsorbed water species. (a) TGA of pristine and 505-day stored NP#8. (b) In-situ DRIFT spectra of 505-day stored NP#8.

stagnation, the effect of water vapor partial pressure, and the existence of chemically adsorbed surface water species were reported. Our observations are consistent with the previous results in ZnO nanoparticles, yet the growth rate of our α-Al$_2$O$_3$ nanoparticles seems to be much slower than the ZnO case, even though the two materials have similar melting points (T_m=2072 $^{\circ}$C for Al$_2$O$_3$ vs. 1975 $^{\circ}$C for ZnO). For example, in our case, NP#1 grows by 1.7 nm (from 3.4 nm to 5.1 nm) in 730 days, compared with a total growth of 3.9 nm for ZnO nanoparticles in 175 days. Assuming a cubic growth law $d_{avg}^3 \sim t$ for both materials, we estimate that the surface diffusivity is about two order of magnitude slower in α-Al$_2$O$_3$ nanoparticles than ZnO nanoparticles at room temperature. While the estimation is rough, it does tell an even more active surface kinetics in "hydrated" ZnO surface than in α-Al$_2$O$_3$. This prediction agrees with the sintering practices of the two materials. Adsorbed water species have been reported to enhance the ZnO sintering, as shown by spark plasma sintering of "humid" ZnO nanoparticles at ≤400 $^{\circ}$C under applied mechanical pressure (50 MPa) and fast heating rate (up to 200 K min^{-1}) [58,59]. With the addition of acetic acid solution and long-time holding using a warm press, ZnO nanoparticles can also be "cold-sintered" to above 90% theoretical density below 300 $^{\circ}$C [47]. In contrast, to date there are no reports on adsorbed water-enhanced sintering in the case of α-Al$_2$O$_3$ and its cold sintering remains challenging. While this indicates different effects of adsorbed water species on α-Al$_2$O$_3$'s surface kinetics compared to ZnO's, the state of the art may also be partially due to the unavailability of commercial ultrafine α-Al$_2$O$_3$ nanoparticles. (Most popular commercial α-Al$_2$O$_3$ fine-powders, such as Taimicron by Taimei Chemicals and AKP series by Sumitomo Chemical, all have particle sizes above 100 nm.) Therefore, encouraged by our new observations of remarkable room-temperature surface kinetics of sub-10 nm α-Al$_2$O$_3$ nanoparticles, we believe that there is plenty of space to explore, from conventional sintering to novel functionality, at ultrafine scale. For example, there may be a substrate effect for α-Al$_2$O$_3$ nanoparticle catalyst support to enhance catalyst activity and durability, and it may be possible to produce high-quality ceramic coating by direct high-velocity nanoparticle impacts. These possibilities will be explored in the future.

8. Conclusions

To summarize, by tracking particle morphology during ambient-condition storage and in-situ TEM deformation experiments, we demonstrated surprisingly active surface diffusion of sub-10 nm α-Al$_2$O$_3$ nanoparticles at room temperature of $0.13T_m$. The high-strain-rate Coble pseudoelasticity indicates that morphological evolution may also be possible under other large external stimuli at macroscopic scales. The higher-temperature annealing experiments show growth stagnation, weak temperature dependence and transition in the growth mechanism of the coarsening kinetics. These observations are related to surface adsorption/desorption of water species and surface relaxation, which are supported by TGA and DRIFT results. To the end, our findings

point out the "living" features of sub-10 nm α-Al$_2$O$_3$ nanoparticles, which can be used beneficially for engineering applications or detrimental as the improperly stored powders may degrade and lose activity.

Declaration of Competing Interest

The authors declare that they have no known competing financial interests or personal relationships that could have appeared to influence the work reported in this paper.

Supplementary materials

Supplementary material associated with this article can be found, in the online version, at doi:10.1016/j.actamat.2023.119038.

References

[1] F.G. Ferré, A. Mairov, L. Ceseracciu, Y. Serruys, P. Trocellier, C. Baumier, O. Kaïtasov, R. Brescia, D. Gastaldi, P. Vena, M.G. Beghi, L. Beck, K. Sridharan, F. D. Fonzo, Radiation endurance in Al$_2$O$_3$ nanoceramics, Sci. Rep. 6 (2016) 33478.

[2] N. Nishiyama, T. Taniguchi, H. Ohfuji, K. Yoshida, F. Wakai, B.-N. Kim, H. Yoshida, Y. Higo, A. Holzheid, O. Beermann, T. Irifune, Y. Sakka, K.-I. Funakoshi, Transparent nanocrystalline bulk alumina obtained at 7.7GPa and 800 $^{\circ}$C, Scripta Mater 69 (2013) 362–365.

[3] A. Krell, P. Blank, H. Ma, T. Hutzler, M. Nebelung, Processing of high-density submicrometer Al$_2$O$_3$ for new applications, J. Am. Ceram. Soc. 86 (2003) 546–553.

[4] B.-N. Kim, K. Hiraga, K. Morita, Y. Sakka, A high-strain-rate superplastic ceramic, Nature 413 (2001) 288–291.

[5] J.P. Buban, K. Matsunaga, J. Chen, N. Shibata, W.Y. Ching, T. Yamamoto, Y. Ikuhara, Grain boundary strengthening in alumina by rare earth impurities, Science 311 (2006) 212–215.

[6] B. Lin, L. Heng, B. Fang, H. Yin, J. Ni, X. Wang, J. Lin, L. Jiang, Ammonia synthesis activity of alumina-supported ruthenium catalyst enhanced by alumina phase transformation, ACS Catal. 9 (2009) 1635–1644.

[7] P.R. Ellis, D.I. Enache, D.W. James, D.S. Jones, G.J. Kelly, A robust and precious metal-free high performance cobalt Fischer-Tropsch catalyst, Nat. Catal. 2 (2019) 623–631.

[8] B.C. Enger, Å.-L. Fossan, Ø. Borg, E. Rytter, A. Holmen, Modified alumina as catalyst support for cobalt in the Fischer-Tropsch synthesis, J. Catal. 284 (2011) 9–22.

[9] J.M. McHale, A. Auroux, A.J. Perrotta, A. Navrotsky, Surface energies and thermodynamic phase stability in nanocrystalline aluminas, Science 277 (1997) 788–791.

[10] M. Yoshida, Y. Kato, Y. Oumi, O. Sakurada, M. Tanaka, M. Wada, S. Kitaoka, Homogeneous nucleation of corundum nanocrystallites by rapid heating of aluminum formate hydroxide-based precursor powder, Sci. Rep. 9 (2019) 14889.

[11] I. Levin, D. Brandon, Metastable alumina polymorphs: crystal structures and transition sequences, J. Am. Ceram. Soc. 81 (1998) 1995–2012.

[12] R.K. Iler, Fibrillar colloidal boehmite; progressive conversion to gamma, theta, and alpha aluminas, J. Am. Ceram. Soc. 44 (1961) 618–624.

[13] R.M. Laine, J.C. Marchal, H.P. Sun, X.Q. Pan, Nano-α-Al$_2$O$_3$ by liquid-feed flame spray pyrolysis, Nat. Mater. 5 (2006) 710–712.

[14] P. Su, X. Guo, S. Ji, Effects of multicomponent catalyzer on preparation of ultrafine α-Al₂O₃ at low sintering temperature, Adv. Powder Technol. 20 (2009) 542–547.

[15] J. Ma, B. Wu, Effect of surfactants on preparation of nanoscale α-Al₂O₃ powders by oil-in-water microemulsion, Adv. Powder Technol. 24 (2013) 354–358.

[16] P.-L. Chang, F.-S. Yen, K.-C. Cheng, H.-L. Wen, Examinations on the critical and primary crystallite sizes during θ-to α-phase transformation of ultrafine alumina powders, Nano Lett. 1 (2001) 253–261.

[17] S. Pu, L. Li, J. Ma, F. Lu, J. Li, Disperse fine equiaxed alpha alumina nanoparticles with narrow size distribution synthesised by selective corrosion and coagulation separation, Sci. Rep. 5 (2015) 11575.

[18] A.P. Amrute, Z. Łodziana, H. Schreyer, C. Weidenthaler, F. Schüth, High-surface-area corundum by mechanochemically induced phase transformation of boehmite, Science 366 (2019) 485–489.

[19] L. Li, S. Pu, Y. Liu, L. Zhao, J. Ma, J. Li, High-purity disperse α-Al₂O₃ nanoparticles synthesized by high-energy ball milling, Adv. Powder Technol. 29 (2018) 2194–2203.

[20] J. Li, S. Pu, W. Cao, L. Li, R. Guo, Comment on "High-surface-area corundum by mechanochemically induced phase transformation of boehmite, Science 368 (2020) eabb0142.

[21] W. Cao, X. Mao, Y. Yuan, L. Li, L. Zhao, J. Li, Sintering kinetics of disperse ultrafine equiaxed α-Al₂O₃ nanoparticles, J. Eur. Ceram. Soc. 37 (2017) 4005–4013.

[22] H. Yang, L. Li, W. Cao, Y. Liu, M. Mukhtar, L. Zhao, Y. Kang, Y. Dong, J. Li, Sintering kinetics and microstructure evolution in α-Al₂O₃ nanocrystalline ceramics: insensitive to Fe impurity, J. Eur. Ceram. Soc. 40 (2020) 1505–1512.

[23] Y. Dong, H. Yang, L. Zhang, X. Li, D. Ding, X. Wang, J. Li, J. Li, I. Chen, Ultra-uniform nanocrystalline materials via two-step sintering, Adv. Funct. Mater. 31 (2021) 2007750.

[24] H. Yang, L. Li, Y. Li, B. Shen, Y. Kang, L. Zhao, J. Li, Y. Dong, Unveiling exceptional sinterability of ultrafine α-Al₂O₃ nanopowders, J. Mater. 7 (2021) 837–844.

[25] A.P. Amrute, K. Jeske, Z. Łodziana, G. Prieto, F. Schüth, Hydrothermal stability of high-surface-area α-Al₂O₃ and its use as a support for hydrothermally stable Fischer-Tropsch synthesis catalysts, Chem. Mater. 32 (2020) 4369–4374.

[26] Y. Lu, J.Y. Huang, C. Wang, S. Sun, J. Lou, Cold welding of ultrathin gold nanowires, Nat. Nanotechnol. 5 (2010) 218–224.

[27] L. Zhang, Y. Tang, Q. Peng, T. Yang, Q. Liu, Y. Wang, Y. Li, C. Du, Y. Sun, L. Cui, F. Yang, T. Shen, Z. Shan, J. Huang, Ceramic nanowelding, Nat. Commun. 9 (2018) 96.

[28] I.M. Lifshitz, V.V. Slyozov, The kinetics of precipitation from supersaturated solid solutions, J. Phys. Chem. Solids 19 (1961) 35–50.

[29] C.Z. Wagner, Theorie der alterung von niederschlägen durch umlösen (Ostwald-reifung), Berichte der Bunsengesellschaft für Physikalische Chemie 65 (1961) 581–591.

[30] B. Dargatz, J. Gonzalez-Julian, O. Guillon, Anomalous coarsening of nanocrystalline zinc oxide particles in humid air, J. Cryst. Growth 419 (2015) 69–78.

[31] P. Fielitz, K. Kelm, R. Bertram, A.H. Chokshi, G. Borchardt, Aluminium-26 grain boundary diffusion in pure and Y-doped polycrystalline α-alumina, Acta Mater 127 (2017) 302–311.

[32] D. Prot, M.le Gall, B. Lesage, A.M. Huntz, C. Monty, Self-diffusion in α-Al₂O₃. IV. Oxygen grain-boundary self-diffusion in undoped and yttria-doped alumina polycrystals, Phil. Mag. A 73 (1996) 935–949.

[33] Y. Oishi, W.D. Kingery, Self-diffusion of oxygen in single crystal and polycrystalline aluminum oxide, J. Chem. Phys. 33 (1960) 480–486.

[34] A.E. Paladino, W.D. Kingery, Aluminum ion diffusion in aluminum oxide, J. Chem. Phys. 37 (1962) 957–962.

[35] D.J. Reed, B.J. Wuensch, Ion-probe measurement of oxygen self-diffusion in single-crystal Al₂O₃, J. Am. Ceram. Soc. 63 (1980) 88–92.

[36] D. Prot, C. Monty, Self-diffusion in α-Al₂O₃. II. Oxygen diffusion in 'undoped' single crystals, Phil. Mag. A 73 (1996) 899–917.

[37] A.H. Heuer, Oxygen and aluminum diffusion in α-Al₂O₃: how much do we really understand? J. Eur. Ceram. Soc. 28 (2008) 1495–1507.

[38] J. Sun, L. He, Y.-C. Lo, T. Xu, H. Bi, L. Sun, Z. Zhang, S.X. Mao, J. Li, Liquid-like pseudoelasticity of sub-10-nm crystalline silver particles, Nat. Mater. 13 (2014) 1007–1012.

[39] Y. Yang, A. Kushima, W. Han, H. Xin, J. Li, Liquid-like, self-healing aluminum oxide during deformation at room temperature, Nano Lett. 18 (2018) 2492–2497.

[40] E.J. Frankberg, J. Kalikka, F.G. Ferré, L. Joly-Pottuz, T. Salminen, J. Hintikka, M. Hokka, S. Koneti, T. Douillard, B.L. Saint, P. Kreiml, M.J. Cordill, T. Epicier, D. Stauffer, M. Vanazzi, L. Roiban, J. Akola, F.D. Fonzo, E. Levänen, K. Masenelli-Varlot, Highly ductile amorphous oxide at room temperature and high strain rate, Science 366 (2019) 864–869.

[41] N.A. Gjostein, Surfaces and interfacesI: Chemical and Physical Characteristics, Syracuse University, New York, 1976.

[42] H.P. Bonzel, Structure and Properties of Metal Surfaces, Maruzen, Tokyo, 1973.

[43] R. Wang, S. Boyd, P.V. Bonnesen, V. Augustyn, Effect of water in a non-aqueous electrolyte on electrochemical Mg²⁺ insertion into WO₃, J. Power Sources 477 (2020), 229015.

[44] Y. Xi, Q. Zhang, H. Cheng, Mechanism of hydrogen spillover on WO₃(001) and formation of HₓWO₃ (x = 0.125, 0.25, 0.375, and 0.5), J. Phys. Chem. C 118 (2014) 494–501.

[45] C.W. Snyder, B.G. Orr, D. Kessler, L.M. Sander, Effect of strain on surface morphology in highly strained InGaAs films, Phys. Rev. Lett. 66 (1991) 3032–3035.

[46] G.J. Whaley, P.I. Cohen, Relaxation of strained InGaAs during molecular beam epitaxy, Appl. Phys. Lett. 57 (1990) 144–146.

[47] S. Funahashi, J. Guo, H. Guo, K. Wang, A.L. Baker, K. Shiratsuyu, C.A. Randall, Demonstration of the cold sintering process study for the densification and grain growth of ZnO ceramics, J. Am. Ceram. Soc. 100 (2017) 546–553.

[48] H.A. Al-Abadleh, V.H. Grassian, FT-IR study of water adsorption on aluminum oxide surfaces, Langmuir 19 (2003) 341–347.

[49] J. Paul, F.M. Hoffmann, Decomposition of water on clean and oxidized aluminum (100), J. Phys. Chem. 21 (1986) 5321–5324.

[50] P.A. Thiel, T.E. Madey, The interaction of water with solid surfaces: fundamental aspects, Surf. Sci. Rep. 7 (1987) 211–385.

[51] J.G. Chen, J.E. Crowell, J.T. Yates Jr, Assignment of a surface vibrational mode by chemical means: modification of the lattice modes of Al₂O₃ by a surface reaction with H₂O, J. Chem. Phys. 84 (1986) 5906–5909.

[52] D.B. Almy, D.C. Foyt, J.M. White, Experimental and theoretical studies of electron binding energies for water adsorbed on α-alumina, J. Electron. Spectrosc. 11 (1977) 129–136.

[53] P.J. Eng, T.P. Trainor, G.E. Brown Jr, G.A. Waychunas, M. Newville, S.R. Sutton, M.L. Rivers, Structure of the hydrated α-Al₂O₃ (0001) surface, Science 288 (2000) 1029–1033.

[54] K.C. Hass, W.F. Schneider, A. Curioni, W. Andreoni, The chemistry of water on alumina surfaces: reaction dynamics from first principles, Science 282 (1998) 265–268.

[55] M. Ali, M. Winterer, ZnO nanocrystals: surprisingly 'alive', Chem. Mater. 22 (2010) 85–91.

[56] L. Liao, H.B. Lu, J.C. Li, H. He, D.F. Wang, D.J. Fu, C. Liu, W.F. Zhang, Size dependence of gas sensitivity of ZnO nanorods, J. Phys. Chem. C 111 (2007) 1900–1903.

[57] A. Tsukazaki, A. Ohtomo, T. Onuma, M. Ohtani, T. Makino, M. Sumiya, K. Ohtani, S.F. Chichibu, S. Fuke, Y. Segawa, H. Ohno, H. Koinuma, M. Kawasaki, Repeated temperature modulation epitaxy for p-type doping and light-emitting diode based on ZnO, Nat. Mater. 4 (2005) 42–46.

[58] S. Schwarz, A.M. Thron, J. Rufner, K. Benthem, O. Guillon, Low temperature sintering of nanocrystalline zinc oxide: effect of heating rate achieved by field assisted sintering/spark plasma sintering, J. Am. Ceram. Soc. 95 (2012) 2451–2457.

[59] B. Dargatz, J. Gonzalez-Julian, M. Bram, P. Jakes, A. Besmehn, L. Schade, R. Röder, C. Ronning, O. Guillon, FAST/SPS sintering of nanocrystalline zinc oxide-Part I: enhanced densification and formation of hydrogen-related defects in presence of adsorbed water, J. Eur. Ceram. Soc. 36 (2016) 1207–1220.

Supplementary information

Evolving corundum nanoparticles at room temperature

Hongbing Yang[1,†], Baoming Wang[2,†], Hong Zhang[3], Bing Shen[1], Yuanyuan Li[1], Ming Wang[1],

Jianjun Wang[1], Wensheng Gao[4], Yueming Kang[1], Lu Li[1], Yanhao Dong[5,*], Jiangong Li[1,*], Ju Li[2,6,*]

[1]Institute of Materials Science and Engineering, School of Materials and Energy, Lanzhou University, Lanzhou 730000, China

[2]Department of Materials Science and Engineering, Massachusetts Institute of Technology, Cambridge, MA 02139, USA

[3]Electron Microscopy Centre of Lanzhou University, School of Materials and Energy, Lanzhou University, Lanzhou730000, China

[4]College of Chemistry and Chemical Engineering, Lanzhou University, Lanzhou730000, China

[5]State Key Laboratory of New Ceramics and Fine Processing, School of Materials Science and Engineering, Tsinghua University, Beijing 100084, China

[6]Department of Nuclear Science and Engineering, Massachusetts Institute of Technology, Cambridge, MA 02139, USA

Table of contents

Supplementary Note S1. Measurements and calculations of particle sizes, size distributions and aspect ratios of particles.

Particle sizes and size distributions were measured along the longest direction over >500 particles from TEM images using a Nano Measurer software. An example of the measurement process is shown in **Supplementary Figure S2**. Aspect ratios of the particles were calculated as the ratio of the longest and shortest directional dimensions of each particle measured by Nano Measurer software. Over >300 particles were calculated to obtain the aspect ratio of the particles for each batch of α-Al_2O_3 nanoparticles.

Supplementary Note S2. Estimation of the average grain size and micro-strain by Halder-Wagner's method.

For nanoparticles, especially those powders after ball milling, the broadening of Bragg diffraction peaks (β_{total}) mainly comes from three parts [S1], the instrumental broadening (β_{instr}), size broadening (β_{size}) caused by grain refinement and micro-strain broadening (β_{strain}) caused by crystal imperfection and distortion. The combination of size broadening β_{size} and micro-strain broadening β_{strain} is also called physical broadening (β). The diffraction peaks profiles for our powders and the silicon reference sample have a Gaussian component, and for this, the following equations are applicable [S2]:

$$\beta_{\text{total}}{}^2 = \beta^2 + \beta_{\text{instr}}{}^2 = \beta_{\text{size}}{}^2 + \beta_{\text{strain}}{}^2 + \beta_{\text{instr}}{}^2 \tag{S1}$$

The instrumental contribution to peak broadening was estimated from the silicon data to be

$$\beta_{\text{instr}} = 0.00297 - 2.83373 \times 10^{-5} \times (2\theta) + 2.4088 \times 10^{-7} \times (2\theta)^2 \tag{S2}$$

where 2θ is the diffraction angle in radians. Since the line profiles broadened by micro-strains β_{strain} can be represented to a good approximation by a Gaussian function, and the broadened by grain refinement β_{size} can be represented to a good approximation by a Cauchy function [S3, S4], Halder & Wagner have demonstrated that the integral breadth of a line profile produced by the convolution of a Gaussian profile with a Cauchy profile is [S5]

$$\frac{\beta_{\text{size}}}{\beta} + \left(\frac{\beta_{\text{strain}}}{\beta}\right)^2 = 1 \tag{S3}$$

For the broadening caused by grain refinement was estimated from the Debye-Scherrer's formula as [S6]

$$\beta_{\text{size}} = \frac{k\lambda}{D\cos\theta} \tag{S4}$$

where D = average grain size, k = shape factor (0.89), and λ = wavelength of Cuk_α radiation (0.15406 nm). For the broadening caused by micro-strain (ε) was calculated using the formula [S7]

$$\beta_{\text{strain}} = 4\varepsilon\tan\theta \tag{S5}$$

where β_{strain} is in radians 2θ. By substituting Eq. (S1), Eq. (S4), Eq. (S5) into Eq. (S3) and

rearrangement, a dimensionless function of the broadening is obtained,

$$\frac{\beta_{\text{total}}^2 - \beta_{\text{instr}}^2}{\tan^2 \theta} = \frac{k\lambda}{D} \times \frac{(\beta_{\text{total}} - \beta_{\text{instr}})^{1/2}}{\tan \theta \times \sin \theta} + 16\varepsilon^2 \tag{S6}$$

Eq. (S6) is also called Halder-Wagner (HW) method [S8]. When a plot of $(\beta_{\text{total}}^2 - \beta_{\text{instr}}^2)/\tan^2\theta$ is made against $(\beta_{\text{total}} - \beta_{\text{instr}})^{1/2}/(\tan\theta * \sin\theta)$, the average grain size can be obtained from the slope $(k\lambda)/D$ of straight line and micro-strain can be obtained from the intercept $16\varepsilon^2$.

A representative plot of $(\beta_{\text{total}}^2 - \beta_{\text{instr}}^2)/\tan^2\theta$ against $(\beta_{\text{total}} - \beta_{\text{instr}})^{1/2}/(\tan\theta * \sin\theta)$ is shown in **Supplementary Figure S6**. Using the Halder-Wagner method, the average grain sizes of some batches of α-Al_2O_3 nanoparticles after extended-time storage at ambient conditions (for NP#8, the grain size of as-synthesized was also calculated) were calculated and presented in **Supplementary Table S2**. The calculated average grain sizes of the NP#8 nanoparticles before and after high-temperature annealing under some parameters are shown in **Supplementary Table S4**.

Supplementary Note S3. Specific surface areas of α-Al$_2$O$_3$ nanoparticles.

Specific surface areas of α-Al$_2$O$_3$ nanoparticles were determined by Brunauer-Emmett-Teller (BET) method using N$_2$ adsorption measurement at 77 K on Micrometrics ASAP 2020M surface area analyze. The nanoparticles were degassed at 200 °C for 5 h before the BET measurements. The measured specific surface areas (S_{BET}) of some batches of α-Al$_2$O$_3$ nanoparticles before (i.e., as-synthesized pristine) and after extended-time storage at ambient conditions (including before and after acid etching) are shown in **Supplementary Table S3**. Note that due to the presence of chemically adsorbed water (which is difficult to completely remove even at higher temperatures) on the surface of α-Al$_2$O$_3$ nanoparticles, and the sintering (form densified aggregates) and coarsening of the nanoparticles during the degassing process (i.e., heat treatment), the measured specific surface area of the α-Al$_2$O$_3$ nanoparticles is difficult to agree with (less than) its theoretical specific surface area ($S_{BET}=6/\rho/d_{avg}$, where ρ is the density of α-Al$_2$O$_3$ taking 3.96 g/cm^3 and d_{avg} is the average particle size).
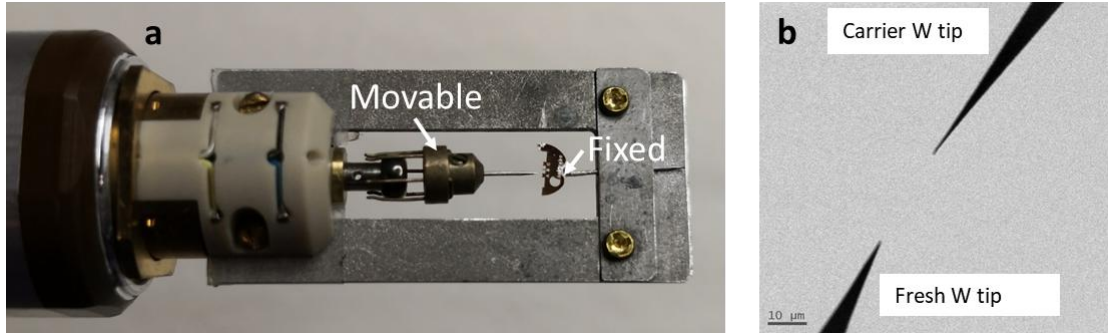
Supplementary Figure S1 Image of (a) the customer-modified Nanofactory TEM holder, and (b) the two W tips for in-situ deformation experiments.
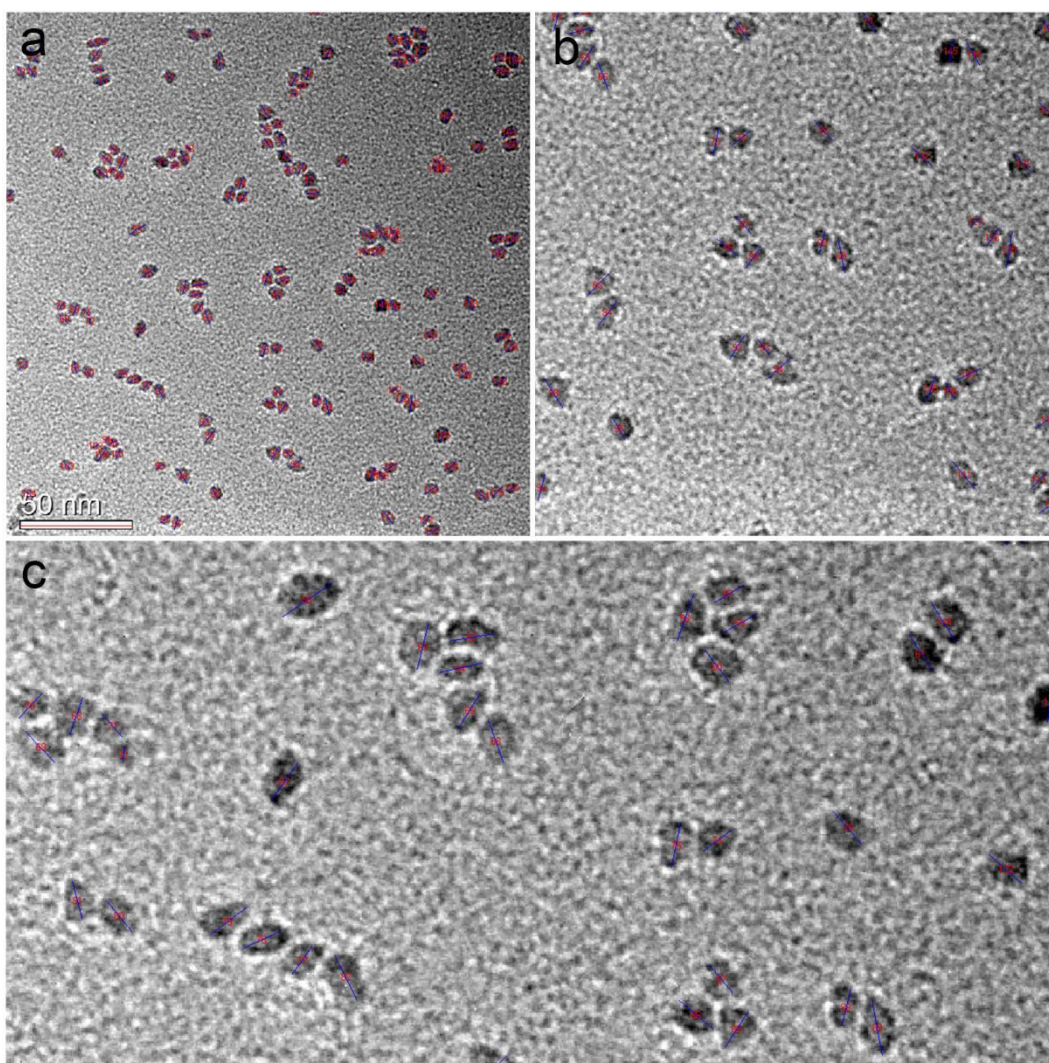
Supplementary Figure S2 An example of using a Nano Measurer software to measure particle size and size distribution. The α-Al$_2$O$_3$ nanoparticles shown here is 850-day stored NP#3 after acid etching.
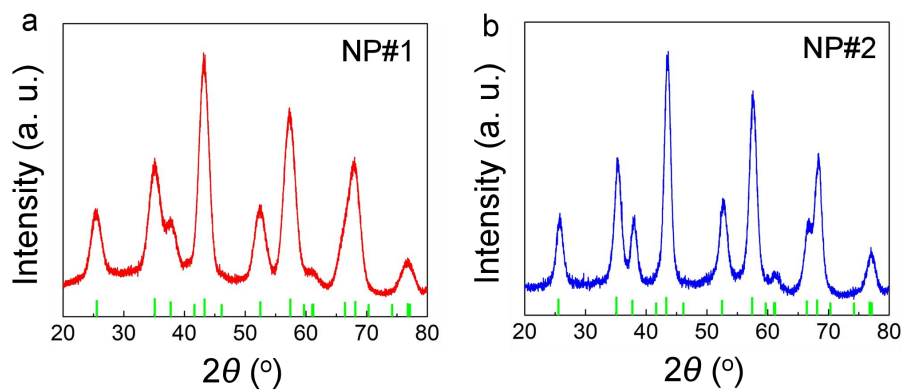
Supplementary Figure S3 XRD of (a) NP#1 and (b) NP#2 after 730-day storage. Both patterns match the reference of α-Al$_2$O$_3$ phase plotted in green.
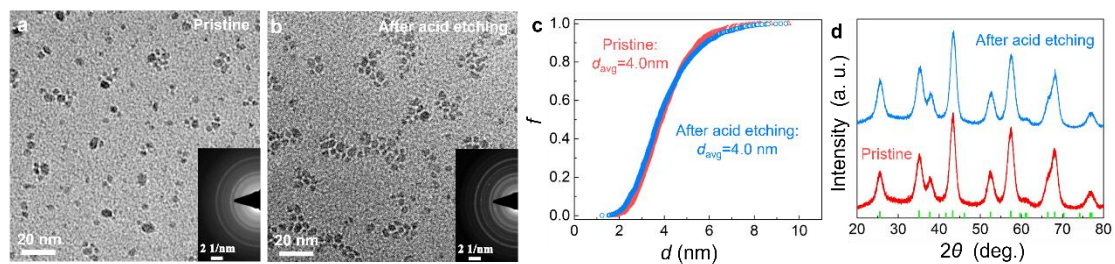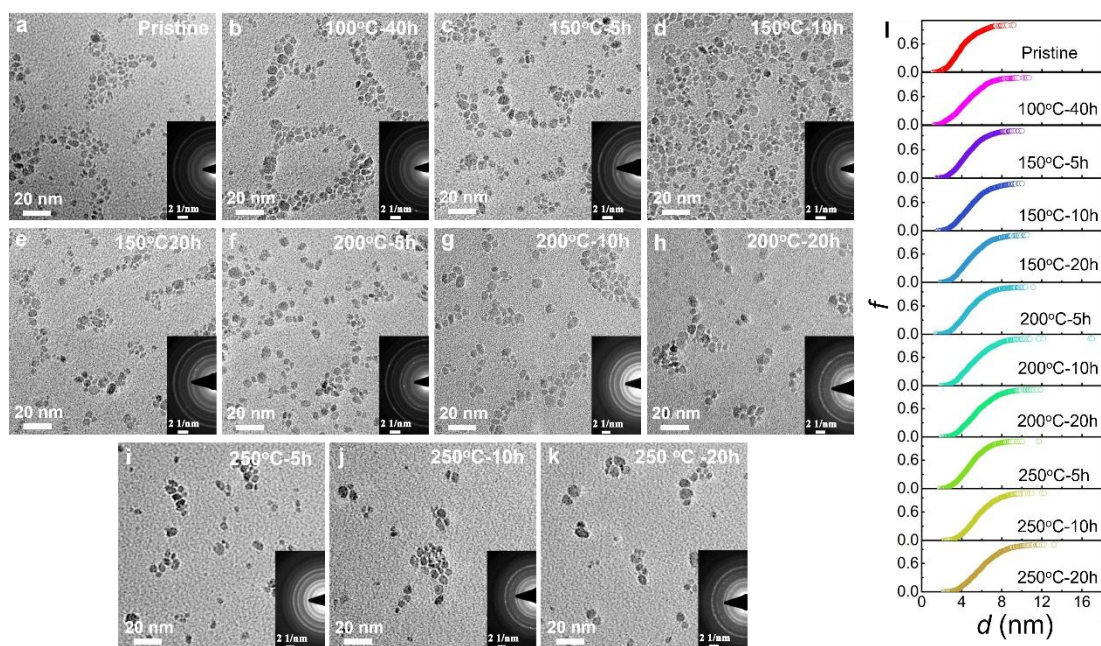
Supplementary Figure S4 Morphology of (a) pristine NP#8 and (b) NP#8 after acid etching at room temperature. (c) Particle size distributions and (d) XRD of the two materials show that the acid etching process does not alter the size and crystallinity of α-Al_2O_3 nanoparticles. Insets of (a,b): SAED patterns confirming α-Al_2O_3 phase for both samples.
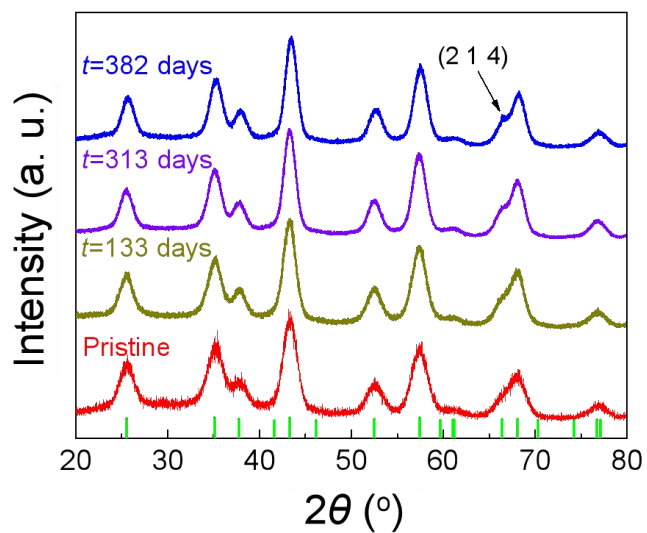
Supplementary Figure S5 XRD of as-synthesized pristine and stored NP#8. All the patterns match the reference pattern of α-Al_2O_3 phase in green.
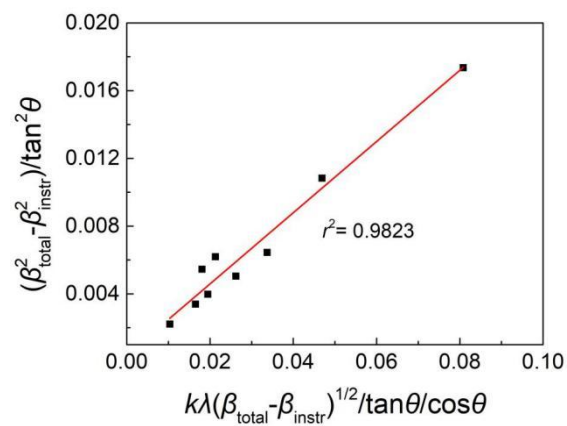
Supplementary Figure S6 A representative Halder-Wagner plot of $(\beta_{total}^2 - \beta_{instr}^2)/\tan^2\theta$ against $(\beta_{total} - \beta_{instr})^{1/2}/(\tan\theta * \sin\theta)$. The data shown here were calculated from the XRD of NP#8 after 313-day storage.
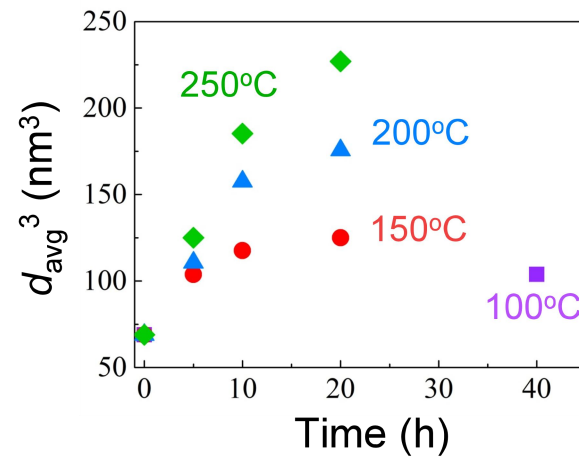
Supplementary Figure S7 Morphology of NP#8 (a) in pristine state, and heat-treated at (b) 100 ℃ for 40 h, (c) 150 ℃ for 5 h, (d) 150 ℃ for 10 h, (e) 150 ℃ for 20 h, (f) 200 ℃ for 5 h, (g) 200 ℃ for 10 h, (h) 200 ℃ for 20 h, (i) 250 ℃ for 5 h, (j) 250 ℃ for 10 h, (k) 250 ℃ for 20 h, and (l) their particle size distributions. Insets of (a-k): SAED patterns confirming α-Al$_2$O$_3$ phase for all samples. All samples (expect for the pristine one) were acid-etched at room temperature before TEM measurements.
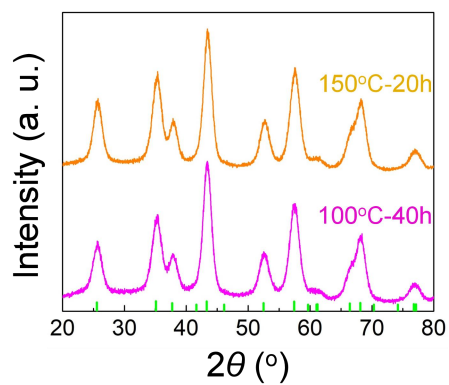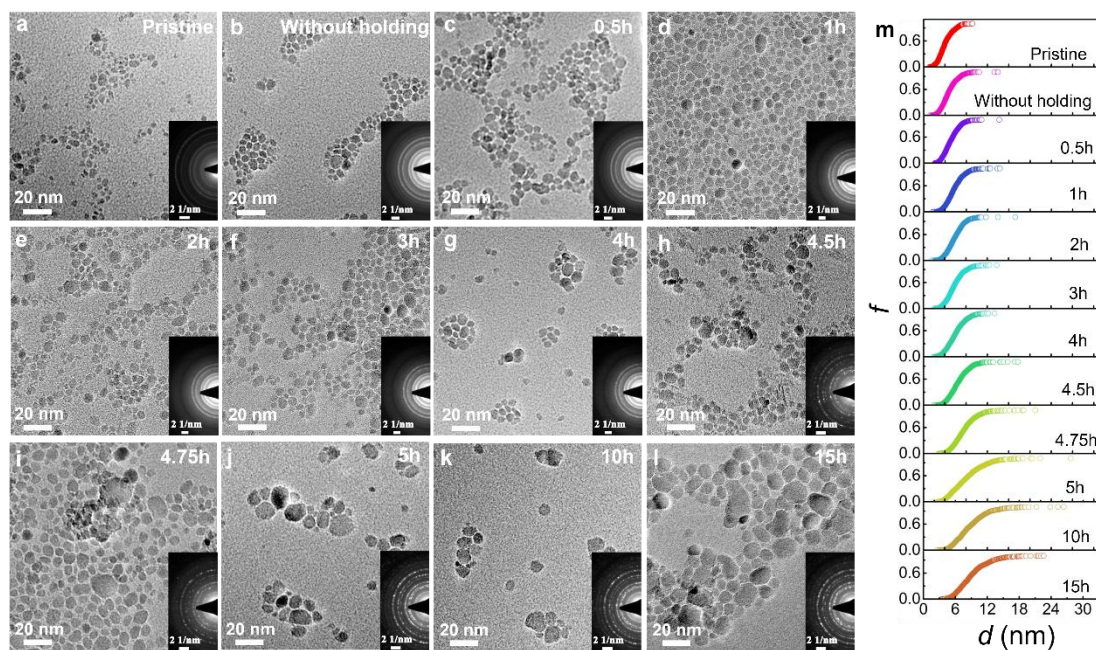
Supplementary Figure S8 XRD of NP#8 heat-treated at 100 °C for 40 h and 150 °C for 20 h.

Both patterns match the reference of α-Al_2O_3 phase plotted in green.

Supplementary Figure S9 $d_{avg}{}^3$ plotted against annealing time at 100 ℃, 150 ℃, 200 ℃, and 250 ℃ of NP#8.

Supplementary Figure S10 Morphology of NP#8 (a) in pristine state, and heat-treated at 600 °C (b) without holding, (c) for 0.5 h, (d) for 1 h, (e) for 2 h, (f) for 3 h, (g) for 4 h, (h) for 4.5 h, (i) for 4.75 h, (j) for 5 h, (k) for 10 h, and (l) for 15 h, and (m) their particle size distributions. Insets of (a-l): SAED patterns confirming α-Al_2O_3 phase for all samples. All samples (expect for the pristine one) were acid-etched at room temperature before TEM measurements.

Supplementary Figure S11 Morphology of NP#8 (a) in pristine state, and heat-treated at 700 °C (b) without holding, (c) for 0.5 h, (d) for 1 h, (e) for 2 h, (f) for 3 h, (g) for 4 h, (h) for 4.5 h, (i) for 4.75 h, (j) for 5 h, (k) for 10 h, and (l) for 15 h, and (m) their particle size distributions. Insets of (a-l): SAED patterns confirming α-Al_2O_3 phase for all samples. All samples (expect for the pristine one) were acid-etched at room temperature before TEM measurements.

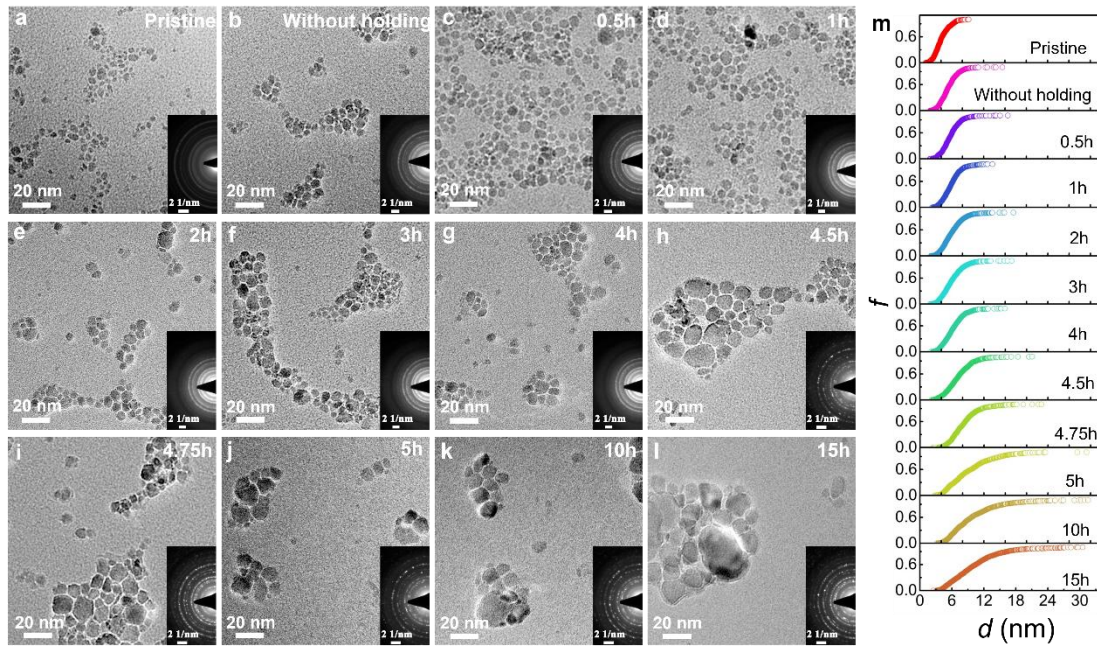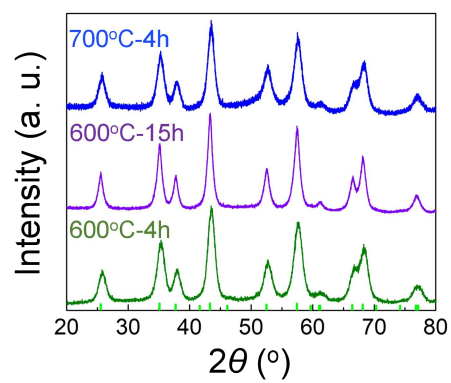**Supplementary Figure S12** XRD of NP#8 heat-treated at 600 °C for 4 h, 600 °C for 15 h, and 700 °C for 4 h. All patterns match the reference of α-Al_2O_3 phase plotted in green.

Supplementary Table S1 Number N of measured particles, average particle size d_{avg}, standard deviation σ of normalized particle size (normalized by d_{avg}), skewness SK of the normalized particle size distribution, and average aspect ratio AR of pristine α-Al_2O_3 nanoparticles and stored ones after storage time t.

	Pristine					After storage					
	N	d_{avg} (nm)	σ	SK	AR	t (days)	N	d_{avg} (nm)	σ	SK	AR
NP#1	1474	3.4	0.27	0.68	1.47	730	869	5.1	0.20	−0.26	1.29
NP#2	1614	5.0	0.30	0.82	1.36	730	754	6.7	0.25	0.56	1.29
NP#3	1292	3.7	0.29	0.69	1.37	850	900	5.7	0.26	0.20	1.29
NP#4	1225	5.2	0.31	0.89	1.34	960	1031	6.7	0.28	0.45	1.31
NP#5	1398	6.7	0.34	0.25	1.40	850	1108	8.6	0.33	0.33	1.28
NP#6	1214	6.3	0.46	0.54	1.48	730	1737	8.5	0.34	0.59	1.43
NP#7	931	10.5	0.49	1.09	1.45	730	1384	11.2	0.48	0.93	1.36
NP#8	1478	4.0	0.31	0.77	1.51	133	1237	4.8	0.29	0.57	1.43
						313	953	5.2	0.28	0.76	1.38
						382	2366	5.3	0.30	0.63	1.35
NP#9	1255	4.3	0.35	0.67	1.46	140	1322	4.7	0.26	0.35	1.34
						325	1604	5.5	0.27	0.52	1.34
						390	1601	5.7	0.28	0.55	1.30

Supplementary Table S2 Average grain sizes D of α-Al_2O_3 nanoparticles before and/or after storage time t in ambient atmosphere at room temperature. (t=0 day refers to as-synthesized pristine nanoparticles.)

	t (days)	D (nm)
NP#1	730	4.0±0.1
NP#2	730	5.9±0.1
NP#3	850	5.1±0.2
NP#4	960	6.0±0.1
NP#6	730	7.0±0.1
NP#8	0	4.2±0.1
	133	4.6±0.1
	313	4.8±0.2
	382	4.9±0.1

Supplementary Table S3 The specific surface areas (S_{BET}) of pristine α-Al$_2$O$_3$ nanoparticles and stored ones after storage time t (including before and after acid etching).

	Pristine		After storage	
			Before acid etching	After acid etching
	S_{BET} (m^2/g)	t (days)	S_{BET} (m^2/g)	S_{BET} (m^2/g)
NP#1	210	730	117	187
NP#2	184	730	87	163
NP#5	176	850	/	156

Supplementary Table S4 Heat treatment temperature, holding time and average grain sizes D of NP#8 before and after being heat-treated at different parameters. Data on the first row are for the as-synthesized pristine NP#8.

Temperature (^{o}C)	Holding time (h)	D (nm)
/	/	4.2±0.1
100	40	4.5±0.1
150	20	4.6±0.1
600	4	5.7±0.2
	15	9.0±0.1
700	4	6.5±0.2

Supplementary Video S1 In-situ TEM deformation experiment on α-Al_2O_3 nanoparticles. The top W tip is the carrier tip. The bottom W tip is a fresh tip for deformation. Video plays at ×16 speed of real time.

Supplementary Video S2 α-Al_2O_3 nanoparticles show stable size and crystallinity under the same electron beam condition as the in-situ TEM deformation experiments. Video plays at ×16 speed of real time.

Supplementary References

[S1] R. Delhez, T.H. De Keijser, J.I. Langford, D. Louër, E.J. Mittemeijer, E.J. Sonneveld, Crystal imperfection broadening and peak shape in the Rietveld method, Oxford Univ. Press, 1993.

[S2] D. Balzar, S. Popović, Reliability of the simplified integral-breadth methods in diffraction line-broadening analysis, J. Appl. Cryst. 29 (1996) 16-23.

[S3] B.E. Warren, B.L. Averbach, The effect of cold-work distortion on X-ray patterns, J. Appl. Phys. 21 (1950) 595-599.

[S4] B.E. Warren, B.L. Averbach, The separation of stacking fault broadening in cold-worked metals, J. Appl. Phys. 23 (1952) 1059-1059.

[S5] N.C. Halder, C.N.J. Wagner, Separation of particle size and lattice strain in integral breadth measurements, Acta Cryst. 20 (1966) 312-313.

[S6] P. Scherrer, Estimation of the size and internal structure of colloidal particles by means of röntgen, Nachr. Ges. Wiss. Göttingen 2 (1918) 96-100.

[S7] A.R. Stokes, A.J.C. Wilson, The diffraction of X rays by distorted crystal aggregates-I, Proc. Phys. Soc. 56 (1944) 174-181.

[S8] N.C. Halder, C.N.J. Wagner, Analysis of the broadening of powder pattern peaks using variance, integral breadth, and Fourier coefficients of the line profile, Adv. X-Ray Anal. 9 (1966) 91-102.